Nodeless superconductivity and topological nodal states in molybdenum carbide

Tian Shang,[1,*,†] Yuting Wang,[2,3,*] Bochen Yu,[1] Keqi Xia,[1] Darek J. Gawryluk,[4] Yang Xu,[1] Qingfeng Zhan,[1] Jianzhou Zhao,[2,‡] and Toni Shiroka[4,5]

[1]*Key Laboratory of Polar Materials and Devices (MOE), School of Physics and Electronic Science, East China Normal University, Shanghai 200241, China*

[2]*Co-Innovation Center for New Energetic Materials, Southwest University of Science and Technology, Mianyang 621010, People's Republic of China*

[3]*School of Science, Southwest University of Science and Technology, Mianyang 621010, People's Republic of China*

[4]*Center for Neutron and Muon Sciences, Paul Scherrer Institut, CH-5232 Villigen PSI, Switzerland*

[5]*Laboratorium für Festkörperphysik, ETH Zürich, CH-8093 Zürich, Switzerland*

(Received 1 July 2024; accepted 5 August 2024; published 15 August 2024)

The orthorhombic molybdenum carbide superconductor with $T_c = 3.2$ K was investigated by muon-spin rotation and relaxation (μSR) measurements and by first-principles calculations. The low-temperature superfluid density, determined by transverse-field μSR, suggests a fully gapped superconducting state in Mo_2C, with a zero-temperature gap $\Delta_0 = 0.44$ meV and a magnetic penetration depth $\lambda_0 = 291$ nm. The time-reversal symmetry is preserved in the superconducting state, as confirmed by the absence of an additional muon-spin relaxation in the zero-field μSR spectra. Band-structure calculations indicate that the density of states at the Fermi level is dominated by the Mo-4*d* orbitals, which are marginally hybridized with the C-2*p* orbitals over a wide energy range. The symmetry analysis confirms that, in the absence of spin-orbit coupling (SOC), Mo_2C hosts twofold-degenerate nodal surfaces and fourfold-degenerate nodal lines. When considering SOC, the fourfold-degenerate nodal lines cross the Fermi level and contribute to the electronic properties. Our results suggest that, similarly to other phases of carbides, also the orthorhombic transition-metal carbides host topological nodal states and may be potential candidates for future studies of topological superconductivity.

DOI: 10.1103/PhysRevB.110.064510

I. INTRODUCTION

The possibilities offered by topological superconductors, ranging from hosting Majorana fermion quasiparticles to potential applications in topological quantum computing [1–4], have stimulated researchers to explore different routes to realize them. The most obvious approach consists in the introduction of extra carriers into a topological insulator to achieve superconductivity (SC). This route has been frequently attempted in the copper- or strontium intercalated Bi_2Se_3 topological insulator [5–8]. Another approach utilizes the proximity effect between a conventional *s*-wave superconductor and a topological insulator or semiconductor [8,9]. The surface states of a topological insulator can lead to a two-dimensional superconducting state with a $p + ip$ pairing at the interfaces, known to support Majorana bound states at the vortices [10]. For instance, evidence of topological SC has been reported in $NbSe_2/Bi_2(Se,Te)_3$ heterostructures [11,12], where $NbSe_2$ represents a typical fully gapped superconductor.

Despite continued efforts to identify topological SC in accordance with the aforementioned approaches, the intricacy of heterostructure fabrication, the rarity of suitable topological insulators, and the inhomogeneity or disorder effects induced by carrier doping have considerably constrained the investigation and potential applications of topological SC. A more attractive way to achieve them is to combine superconductivity and a nontrivial electronic band structure in the same material. Clearly, it is of fundamental interest to be able to identify such new superconductors with nontrivial band topology, but with a simple composition. For example, topologically protected surface states have been found in superconducting CsV_3Sb_5 [13], β-$PdBi_2$ [14], and $PbTaSe_2$ [15], all of which are good platforms for studying topological SC.

In this respect, the binary transition-metal carbides (TMCs) represent another promising family of materials. TMCs exhibit essentially four different solid phases, which include the α ($Fm\bar{3}m$ No. 225), β ($Pbcn$, No. 60), γ ($P\bar{6}m2$, No. 187), and η ($P6_3/mmc$, No. 194) phases [16]. The γ phase is noncentrosymmetric, while the other three are centrosymmetric. Due to the lack of space inversion, the γ-phase TMCs exhibit exotic topological features. For instance, unconventional three-component fermions with surface Fermi arcs were experimentally observed in γ-phase WC [17]. By applying external pressure, the topological semimetal MoP (isostructural to WC) becomes a superconductor, whose T_c rises up to 4 K (above 90 GPa) [18], thus representing a candidate topological superconductor. Unfortunately, no SC has been observed in WC yet, and the γ-phase MoC (similar to WC and also not superconducting) was predicted to be a topological nodal-line semimetal with drumhead surface states [19]. The α-phase TMCs show relatively high T_c values and some of

*These authors contributed equally to this work.
†Contact author: tshang@phy.ecnu.edu.cn
‡Contact author: jzzhao@swust.edu.cn

them were also predicted to exhibit nontrivial band topologies [16,19–27]. For example, NbC and TaC are fully gapped superconductors with $T_c = 11.5$ and 10.3 K, respectively [25]. At the same time, theoretical calculations suggest that α-phase TMCs are nodal-line semimetals in the absence of spin-orbit coupling (SOC) [19,25].

As for the molybdenum carbides, although their SC was already reported in the 1970s [26], their detailed study was not possible due to difficulties in synthesizing clean samples. Only recently, the α-phase MoC_x ($x < 1$) and η-phase Mo_3C_2 (with $T_c = 14.3$ and 8.5 K) could be synthesized under high-temperature and high-pressure conditions (1700 °C, 6–17 GPa) [28–30] and their superconducting properties studied via different techniques. To date, the electronic properties of the other phases of molybdenum carbides (such as the β phase) remain mostly unexplored.

In this paper, we report on the superconducting properties of the β-phase Mo_2C, investigated via magnetization and muon-spin relaxation and rotation (μSR) measurements. In addition, we also present numerical density-functional-theory (DFT) band-structure calculations. We find that Mo_2C exhibits a fully gapped superconducting state, while its electronic band structure suggests that it hosts twofold-degenerate nodal surfaces and fourfold-degenerate nodal lines. Therefore, the β-phase TMCs (of which Mo_2C is a typical example) may be one of the potential candidates for future studies of topological SC, similar to the other TMC phases.

II. EXPERIMENTAL AND NUMERICAL METHODS

First, we tried to synthesize the β-phase Mo_2C by arc-melting Mo slugs (99.95%, Alfa Aesar) and C rods (99.999+%, ChemPUR). Similarly to previous studies [31], the obtained polycrystalline samples showed a mixture of different phases, both before and after the annealing. Akin to the α-phase, the β-phase Mo_2C can be synthesized also under high-temperature and high-pressure conditions (1500–2300 K, 5 GPa) [32]. However, the resulting Mo_2C samples have a rather low superconducting volume fraction. Because of these issues, all our measurements were performed on high-purity Mo_2C powders (99.5%) produced by Alfa Aesar. For the μSR investigation, the powders were pressed into pellets, while for the magnetization measurements performed on a 7-T Quantum Design magnetic property measurement system loose powders were used. Room-temperature x-ray powder diffraction (XRD) was performed on a Bruker D8 diffractometer using Cu Kα radiation. The μSR measurements were carried out at the multipurpose surface-muon spectrometer (Dolly) at the πE1 beamline of the Swiss muon source at Paul Scherrer Institut (PSI), Villigen, Switzerland. The Mo_2C pellets were mounted on a 25-μm-thick copper foil to cover an area 6–8 mm in diameter. The μSR spectra comprised both transverse-field (TF) and zero-field (ZF) measurements, performed upon heating the sample. The μSR spectra were analyzed by means of the MUSRFIT software package [33].

The phonon spectrum and the electronic band structure of Mo_2C were calculated via DFT, within the generalized gradient approximation (GGA) of the Perdew-Burke-Ernzerhof (PBE) realization [34], as implemented in the Vienna *ab initio* Simulation Package (VASP) [35,36]. The projector augmented wave (PAW) pseudopotentials were adopted for the calculation [37,38]. Electrons belonging to the outer atomic configuration were treated as valence electrons, here corresponding to 6 electrons in Mo ($4d^5 5s^1$) and 4 electrons in C ($2s^2 2p^2$). The kinetic energy cutoff was fixed to 400 eV. For the three different crystal structures of Mo_2C, the atomic positions and the lattice constants were fully relaxed for the calculations of the phonon dispersion spectra. The force convergence criterion was set to 1 meV. For the structure optimization calculations, Monkhorst-Pack grids of $16 \times 16 \times 10$, $14 \times 11 \times 13$, and $19 \times 19 \times 21$ k points were used for the space groups $P6_3/mmc$, $Pbcn$, and $P\bar{3}1m$, respectively. To obtain the force constants and phonon spectra, we used the density functional perturbation theory (DFPT) in combination with the PHONOPY package [39–41]. A supercell of $2 \times 2 \times 2$ was adopted for the calculation of force constants. To calculate the phonon spectrum, the Brillouin zone integration was performed on a Γ-centered mesh of $10 \times 10 \times 7$, $7 \times 5 \times 6$, and $6 \times 6 \times 7$ k points for the space groups $P6_3/mmc$, $Pbcn$, and $P\bar{3}1m$, respectively. In the $P6_3/mmc$ case, considering that only half of the 2a sites are occupied by C atoms, we simplified the structure such that C atoms are fully occupied only at the corners of the unit cell. The spin-orbit coupling (SOC) was fully considered in our calculation. After optimizing the parameters, the electronic and phononic band structures, as well as the density of states (DOS) were calculated.

III. RESULTS AND DISCUSSION

A. Crystal structure

The phase purity and the crystal structure of Mo_2C powders were checked via XRD measurements at room temperature (see Fig. 1). Unlike the arc-melted Mo_2C sample [31], the purchased Mo_2C powders show a clean phase. Several phases of molybdenum carbides have been reported, which exhibit cubic, orthorhombic, hexagonal, and trigonal structures [29,30,32,42,43]. In our case, the XRD pattern of Mo_2C, was analyzed by means of the FullProf Rietveld-analysis suite [44] to find that only the latter three structures, with space groups $Pbcn$ (No. 60, orthorhombic), $P6_3/mmc$ (No. 194, hexagonal), and $P\bar{3}1m$ (No. 162, trigonal) reproduce the data reasonably well. In the insets we depict the corresponding crystal structures, known as β, η, and ζ phases, respectively. Among these, the β phase exhibits the best agreement with the measured XRD pattern, here reflected in the smallest goodness-of-fit factor (see Table I). Moreover, both the η and ζ phases fail to reproduce some of the low-intensity reflections. For instance, as illustrated in the inset of Fig. 1(a), while neither the η nor the ζ phases admit a reflection at $2\theta \approx 30°$, the β phase captures this reflection quite well. In conclusion, the Rietveld refinements suggest that the investigated Mo_2C powders adopt an orthorhombic structure with a space group $Pbcn$, as further confirmed by the calculated phonon-dispersion spectrum (see below). Furthermore, no impurity phases could be detected, indicating a good sample quality. The refined crystal-structure information and atomic coordinates for all the three different phases are listed in Tables I and II.

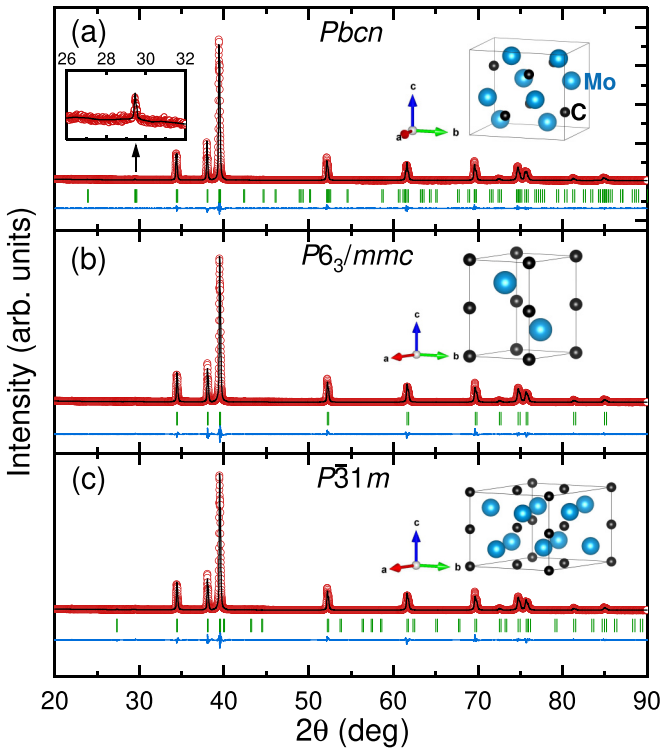

FIG. 1. Room-temperature x-ray powder diffraction patterns and Rietveld refinements for Mo_2C powders using different space groups: *Pbcn* (a), $P6_3/mmc$ (b), and $P\bar{3}m$ (c). The left inset in (a) shows an enlarged plot of intensity for 2θ between 26° and 30°. The open red circles and the solid black lines represent the experimental patterns and the refinement profiles, respectively. The blue lines at the bottom show the residuals, i.e., the difference between the calculated and the experimental data. The vertical bars mark the calculated Bragg-peak positions. The unit-cell crystal structures are shown in the right insets of each panel. Here, the blue and black spheres represent the Mo and C atoms, respectively.

B. Magnetization measurements

We first characterized the SC of Mo_2C powders by magnetic susceptibility, carried out in a 5-mT field, using both field-cooled (FC) and zero-field-cooled (ZFC) protocols. As indicated by the arrow in Fig. 2(a), a clear diamagnetic signal appears below the superconducting transition at $T_c = 3.2$ K. The reduced T_c value compared to the previously reported $T_c \sim 6$ K (whose SC fraction was less than 1%) is most likely

TABLE I. Refined lattice parameters and goodness of fits (including R factors and χ_r^2) for Mo_2C powders utilizing different space groups. The orthorhombic β phase shows clearly the best-fit parameters.

	Pbcn (No. 60)	$P6_3/mmc$ (No. 194)	$P\bar{3}1m$ (No. 162)
Structure	orthorhombic (β phase)	hexagonal (η phase)	trigonal (ζ phase)
a (Å)	4.7332(2)	3.0070(2)	5.2085(2)
b (Å)	6.0292(2)	3.0070(2)	5.2085(2)
c (Å)	5.2055(2)	4.7279(2)	4.7282(2)
V_{cell} (Å^3)	148.553(9)	37.021(3)	111.084(8)
R_P	3.31	4.23	4.24
R_{WP}	4.79	6.37	6.38
R_{exp}	1.82	1.83	1.82
χ_r^2	6.91	12.1	12.2

TABLE II. Refined atomic coordinates and occupations of the three different crystal structures of Mo_2C powders. Only the orthorhombic structure, with *Pbcn* space group, is relevant in our case.

Atom	Wyckoff	x	y	z	Occupation
			Pbcn		
Mo1	8*d*	0.2470(4)	0.1250	0.0798(2)	1
C1	4*c*	0.00000	0.3750(2)	0.2500	1
			$P6_3/mmc$		
Mo1	2*c*	0.3333	0.6667	0.2500	1
C1	2*a*	0.0000	0.0000	0.0000	0.5
			$P\bar{3}1m$		
Mo1	6*k*	0.3333	0.0000	0.2500	1.00
C1	1*a*	0.0000	0.0000	0.0000	0.97
C2	1*b*	0.0000	0.0000	0.5000	0.03
C3	2*c*	0.3333	0.6667	0.0000	0.26
C4	2*d*	0.3333	0.6667	0.5000	0.74

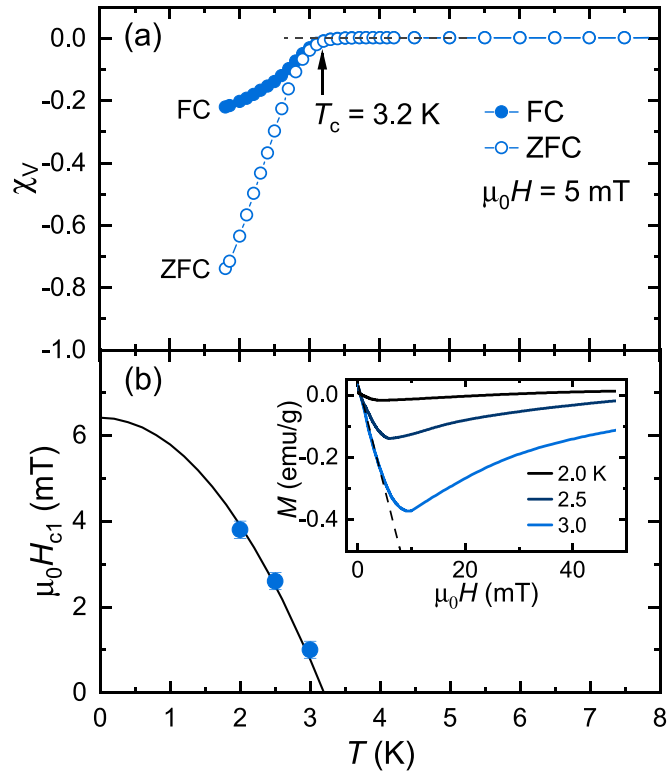

FIG. 2. (a) Magnetic susceptibility of Mo_2C vs temperature, measured in an applied field of 5 mT using both ZFC and FC protocols. (b) Temperature-dependent lower critical field $H_{c1}(T)$ for Mo_2C. The solid line is a fit to $H_{c1}(T) = H_{c1}(0)[1 - (T/T_c)^2]$. Inset: Field-dependent magnetization curves recorded at different temperatures below T_c. The lower critical field H_{c1} was determined as the field value where $M(H)$ starts deviating from linearity (see dashed line).

attributed to the varying C content [32]. Such a variable T_c against C content has been previously reported in the α and η phase of molybdenum carbides [28–30], where the light C atom is expected to modify significantly the electron-phonon coupling and the phonon frequencies and, ultimately, also T_c. A large diamagnetic response (i.e., $\chi_V \sim -0.8$ at 2 K) indicates a bulk SC in Mo_2C, as further confirmed by our TF-μSR measurements. The field-dependent magnetization curves $M(H)$, collected at a few temperatures below T_c, are plotted in the inset of Fig. 2(b). The estimated lower critical fields H_{c1} as a function of temperature are summarized in Fig. 2(b). This yields a lower critical field $\mu_0 H_{c1} = 6.4(2)$ mT for Mo_2C at zero temperature (see solid line).

C. Transverse-field μSR

To study the gap symmetry and superconducting pairing of Mo_2C, we performed systematic TF-μSR measurements in an applied field of 30 mT (i.e., much higher than H_{c1}) at various temperatures. In a TF-μSR measurement, the magnetic field is applied perpendicular to the muon-spin direction, leading to the precession of the muon spin. By performing TF-μSR, one can quantify the additional field-distribution broadening due to the flux-line lattice (FLL) and, thus, determine the superfluid density in type-II superconductors. Figure 3(a) plots two representative superconducting- and normal-state TF-μSR spectra for Mo_2C. The enhanced muon-spin relaxation in the superconducting state is clearly visible and it is due to the formation of a FLL during the field-cooling process, which generates an inhomogeneous field distribution [45–47]. The broadening of the field distribution in the superconducting state is clearly reflected in the fast Fourier transform (FFT) of the TF-μSR spectra [see Figs. 3(b) and 3(c)]. To describe the field distribution, the TF-μSR spectra can be modeled using [48]

$$A_{\mathrm{TF}}(t) = \sum_{i=1}^{n} A_i \cos(\gamma_\mu B_i t + \phi) e^{-\sigma_i^2 t^2/2} + A_{\mathrm{bg}} \cos(\gamma_\mu B_{\mathrm{bg}} t + \phi). \quad (1)$$

Here A_i, A_{bg} and B_i, B_{bg} are the initial asymmetries and local fields sensed by implanted muons in the sample and sample holder, $\gamma_\mu/2\pi = 135.53$ MHz/T is the muon gyromagnetic ratio, ϕ is a shared initial phase, and σ_i is the Gaussian relaxation rate of the ith component. Here, we find that Eq. (1) with $n = 2$ [solid line in Fig. 3(b)] shows a better agreement with the experimental data than with $n = 1$ [dashed line in Fig. 3(b)]. In the normal state, the derived muon-spin relaxation rates $\sigma_i(T)$ are small and independent of temperature while, below T_c, they start to increase due to the onset of the FLL and the increased superfluid density (see inset in Fig. 4). The effective Gaussian relaxation rate σ_{eff} can be calculated from $\sigma_{\mathrm{eff}}^2/\gamma_\mu^2 = \sum_{i=1}^{2} A_i[\sigma_i^2/\gamma_\mu^2 - (B_i - \langle B\rangle)^2]/A_{\mathrm{tot}}$ [48], where $\langle B\rangle = (A_1 B_1 + A_2 B_2)/A_{\mathrm{tot}}$ and $A_{\mathrm{tot}} = A_1 + A_2$. By considering the constant nuclear relaxation rate σ_n in the narrow temperature range (~0.3–5 K) investigated here, confirmed also by ZF-μSR measurements (see Fig. 5). Hence, the superconducting Gaussian relaxation rate can be extracted from $\sigma_{\mathrm{sc}} = \sqrt{\sigma_{\mathrm{eff}}^2 - \sigma_n^2}$.

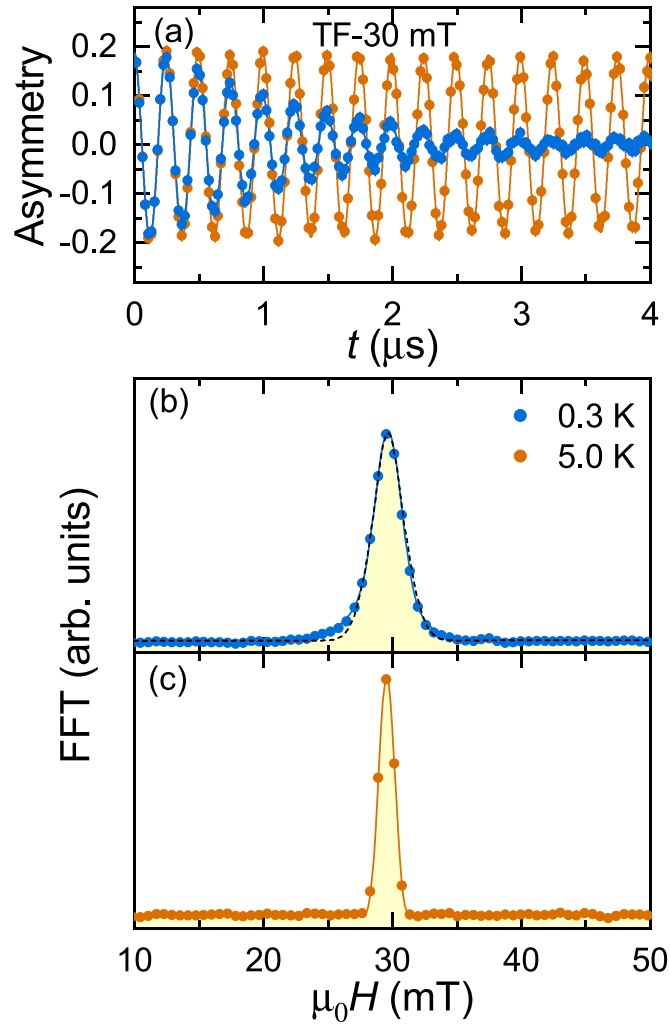

FIG. 3. (a) Representative TF-μSR spectra of Mo_2C collected in its superconducting (0.3 K) and normal state (5 K) in an applied magnetic field of 30 mT. Fast Fourier transforms of the relevant time spectra at (b) 0.3 K and (c) 5 K. The dashed and solid lines are fits to Eq. (1) using one and two oscillations, respectively. Note the clear broadening of field distribution in the superconducting state. Fits with two oscillations show a goodness of fit $\chi_r^2 \sim 1.1$, which is much smaller than $\chi_r^2 \sim 1.7$ of the one-oscillation fits.

The effective magnetic penetration depth λ_{eff} can then be calculated using $\sigma_{\mathrm{sc}}^2(T)/\gamma_\mu^2 = 0.00371\Phi_0^2/\lambda_{\mathrm{eff}}^4(T)$ [49,50]. Figure 4 summarizes the temperature-dependent inverse square of magnetic penetration depth $\lambda_{\mathrm{eff}}^{-2}(T)$, which is proportional to the superfluid density $\rho_{\mathrm{sc}}(T)$. The various models used to analyze the $\rho_{\mathrm{sc}}(T)$ data are generally described by the relation

$$\rho_{\mathrm{sc}}(T) = 1 + 2\left\langle \int_{\Delta_k}^{\infty} \frac{E}{\sqrt{E^2 - \Delta_k^2}} \frac{\partial f}{\partial E} \mathrm{d}E \right\rangle_{\mathrm{FS}}. \quad (2)$$

Here, $f = (1 + e^{E/k_B T})^{-1}$ is the Fermi function and $\langle\,\rangle_{\mathrm{FS}}$ represents an average over the Fermi surface [51]; $\Delta_k(T) = \Delta(T)\delta_k$ is an angle-dependent gap function, where Δ is the maximum gap value and δ_k is the angular dependence of the gap, equal to 1, $\cos 2\phi$, and $\sin\theta$ for an s-, d-, and p-wave

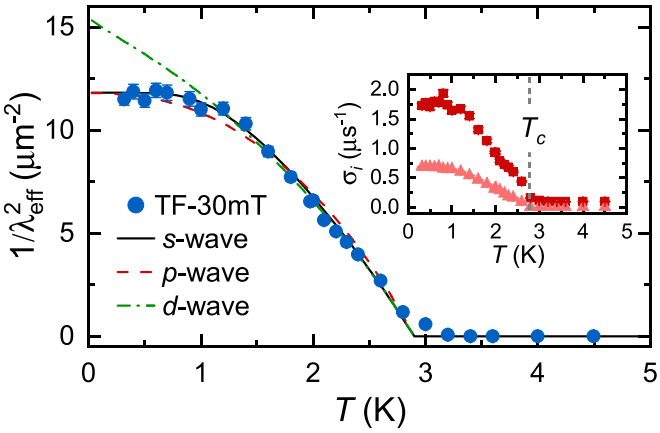

FIG. 4. Temperature-dependent inverse square of the effective magnetic penetration depth of Mo_2C, as determined from TF-μSR measurements in an applied magnetic field of 30 mT. The solid, dashed, and dash-dotted lines represent fits to the s-, p-, and d-wave model, with $\chi_r^2 \sim 1.9$, 5.1, and 14, respectively. The inset shows the two muon-spin relaxation rates $\sigma_i(T)$ required to fit the TF-μSR data, where the dashed line indicates the $T_c = 2.9$ K.

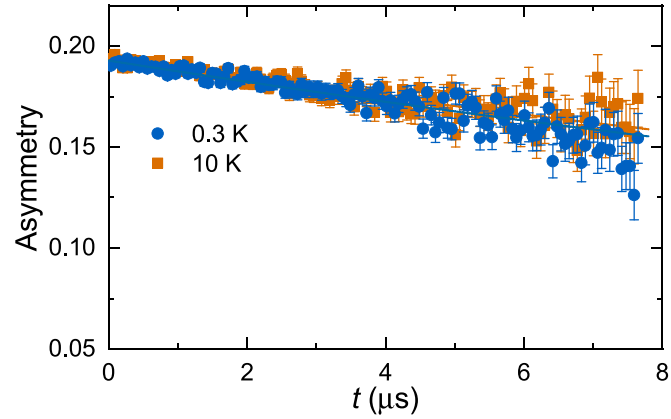

FIG. 5. ZF-μSR spectra of Mo_2C, recorded in its superconducting (0.3 K) and its normal (10 K) states. Solid lines through the data are fits using the Kubo-Toyabe relaxation function.

model, respectively, where ϕ and θ are the azimuthal angles. The temperature-dependent gap is assumed to follow $\Delta(T) = \Delta_0 \tanh\{1.82[1.018(T_c/T - 1)]^{0.51}\}$ [51,52], where Δ_0 is the zero-temperature gap value. The s- and p-wave models (see black solid and red dashed lines in Fig. 4) yield the same zero-temperature magnetic penetration depth $\lambda_0 = 291(3)$ nm, but different zero-temperature energy gaps $\Delta_0 = 0.44(1)$ and 0.60(1) meV, respectively. The magnetic penetration depth of the β-phase Mo_2C is much larger than that of the α-phase MoC_x ($\lambda_0 \sim 132$ nm) and the η-phase Mo_3C_2 ($\lambda_0 \sim 197$ nm) [28,29]. A possible d-wave model (green dash-dotted line in Fig. 4) provides a gap size $\Delta_0 = 0.55(1)$ meV. This is comparable to the p-wave model, but $\lambda_0 = 255(3)$ nm is much shorter than that of both the s- and p-wave models. As can be clearly seen in Fig. 4, below ~1.2 K, the d-wave model deviates significantly from the experimental data. At the same time, also the p-wave model shows a poor agreement with data in the 0.7–1.6 K range. The s-wave model, on the other hand, reproduces the experimental data quite well over the entire temperature range studied. In addition, the temperature-independent $\lambda_{\rm eff}^{-2}(T)$ for $T < 1$ K (i.e., $1/3T_c$) definitely excludes possible gap nodes and suggests that a fully gapped superconducting state occurs in Mo_2C.

D. Zero-field μSR

ZF-μSR is one of the few techniques sensitive enough to detect the tiny spontaneous magnetic field occurring below the superconducting transition temperature. Similarly, it is suitable also for detecting a possible short-range magnetic order or magnetic fluctuations. In view of this, we performed also ZF-μSR measurements on Mo_2C. The ZF-μSR spectra collected in the normal and superconducting states of Mo_2C are presented in Fig. 5. The lack of a fast decay and of coherent oscillations in the ZF-μSR data confirms the absence of magnetic order and/or fluctuations in Mo_2C. As a consequence, owing to the absence of magnetic fields of electronic origin, the muon-spin relaxation is mainly due to the randomly oriented nuclear magnetic moments. Considering that both Mo and C atoms have relatively small nuclear moments (<1 μ_n), Mo_2C exhibits a very weak muon-spin relaxation. Therefore, the ZF-μSR spectra can be modeled by a Lorentzian-type Kubo-Toyabe relaxation function $G_{\rm KT} = [\frac{1}{3} + \frac{2}{3}(1 - \Lambda_{\rm ZF}t)\,{\rm e}^{-\Lambda_{\rm ZF}t}]$ [45,53], where $\Lambda_{\rm ZF}$ represents the zero-field Lorentzian relaxation rate. As shown by solid lines in Fig. 5, the ZF-μSR spectra of Mo_2C were fitted to $A_{\rm ZF}(t) = A_s G_{\rm KT} + A_{\rm bg}$, where A_s is the same as A_i in Eq. (1). The obtained muon-spin relaxation rates are $\Lambda_{\rm ZF} = 0.021(1)$ μs^{-1} at 0.3 K and 0.019(1) μs^{-1} at 10 K. Obviously, the relaxation rates are almost identical in the superconducting and the normal state of Mo_2C, differing less than their standard deviations. The absence of an additional muon-spin relaxation below T_c definitely excludes a possible time-reversal symmetry (TRS) breaking in the superconducting state of Mo_2C. Hence, combined with TF-μSR data, our ZF-μSR results suggest a conventional fully gapped bulk SC with a preserved TRS in the β-phase Mo_2C superconductor.

E. Band-structure calculations

According to the XRD refinements (see Fig. 1), in Mo_2C, the orthorhombic crystal structure shows the best agreement with the XRD pattern. To confirm the crystal structure of Mo_2C, we performed comparative first-principles calculations of the phonon dispersion spectra of Mo_2C by using the space groups $Pbcn$ (β phase), $P6_3/mmc$ (η phase), and $P\bar{3}1m$ (ζ phase), respectively. As shown in Figs. 6(a)–6(c), no soft phonon modes could be identified in the spectra of these structures, implying that all of them are dynamically stable and can be synthesized experimentally. This is consistent with the mixture of different phases we found in the samples obtained by arc melting. The calculated total energies versus the unit-cell volumes are summarized in Fig. 6(d) for the three crystal structures. Among them, the β-phase Mo_2C has the lowest energy at the equilibrium volume, while this is highest for the η-phase. Therefore, the β-phase molybdenum carbides can be stabilized at a relatively low pressure and temperature compared to the other phases [28–30,32]. Since both the

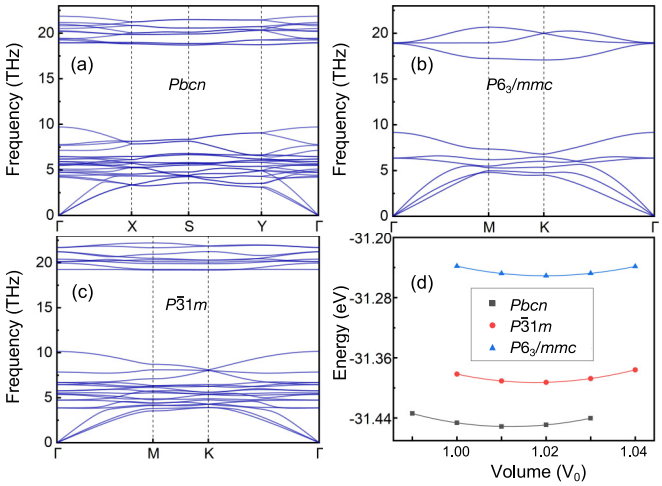

FIG. 6. The calculated phonon dispersion spectra for the β (a), η (b), and ζ phase (c) of Mo_2C. The calculated total energies vs unit-cell volume for the three crystal structures are shown in (d). Here, V_0 stands for the experimental volume (see details in Table I).

theory and the experiment confirm that Mo_2C adopts the β phase, we calculated the electronic band structures solely for this phase. The theoretical results for the other phases can be found elsewhere [19,23,54].

The calculated electronic band structures for the β-phase Mo_2C are summarized in Fig. 7. Close to the Fermi level, the electronic bands are dominated by the 4*d* orbitals of Mo atoms, while the contribution from the C-2*p* orbitals is almost negligible. Indeed, over a wide range of energies, the contribution from the C-2*p* orbitals is less than 4.4%. This situation is also reflected in the DOS shown in the right panels. The estimated DOS at the Fermi level is about 1.93 states/(eV f.u.) [=7.72 states/(eV cell)/Z, with $Z = 4$, the number of Mo_2C formula units per unit cell]. Such a relatively high DOS suggests a good metallicity for Mo_2C, consistent with previous electrical resistivity data [32]. After including the SOC the bands separate, since it breaks the band degeneracy and brings one of the bands closer to the Fermi level [see Fig. 7(b)]. The band splitting due to the SOC is rather weak, here visible only along the *Z*-*U* line near the Fermi level. Although the band splitting along the *S*-*Y* line is quite significant, these bands are too far away from the Fermi level to have any meaningful influence on the electronic properties of Mo_2C. In the β-phase Mo_2C, the band splitting E_{SOC} is up to 100 meV. This is comparable to that in the α-phase NbC, but much smaller than in the TaC [25].

The *Pbcn* space group of Mo_2C is nonsymmorphic and it has an inversion symmetry. After inspecting the band structure without SOC across the whole Brillouin zone [see Fig. 7(a)], the bands along the *X*-*S*-*Y*, *Z*-*U*, and *R*-*T*-*Z* directions turn out to be twofold degenerate, while the bands along *U*-*R* are fourfold degenerate (without considering the spin degree of freedom). By using symmetry arguments [55], the *X*-*U*-*S*-*R* and *U*-*R*-*Z*-*T* planes are twofold-degenerate nodal surfaces due to the combined presence of a screw rotation and time-reversal symmetries. The fourfold-degenerate nodal lines along *U*-*R* are protected by the combination of glide-mirror and *PT* symmetries. In the

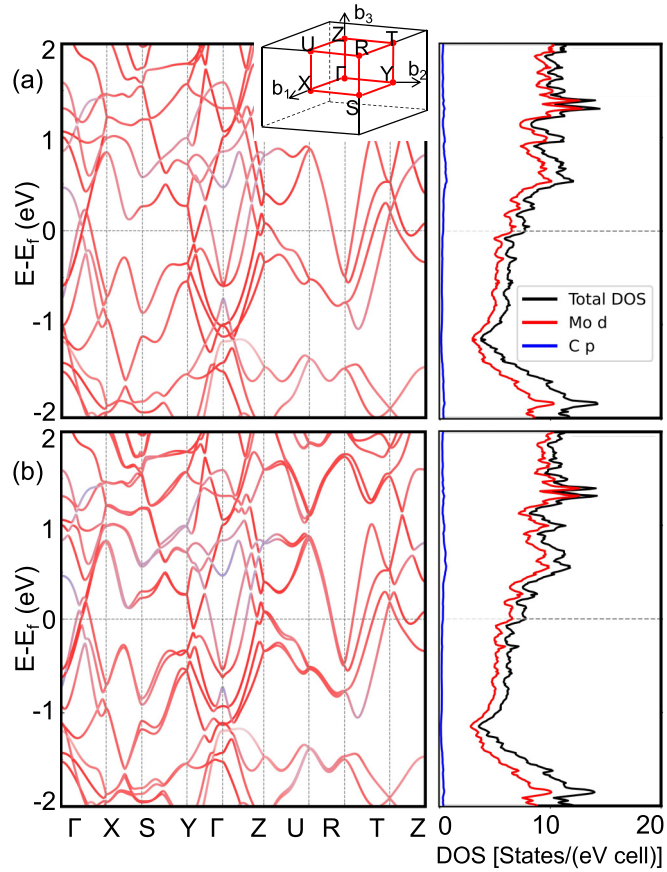

FIG. 7. Electronic band structures of Mo_2C calculated by ignoring (a) and by considering (b) the spin-orbit coupling. Here, the Mo-*d* orbitals and the C-*p* orbitals are shown in red and blue, respectively. The total and partial (Mo and C atoms) densities of states without SOC and with SOC are shown on the right side of each panel. The primitive-cell Brillouin zone, including the high-symmetry points, is shown in the inset of panel (a).

presence of SOC, the fourfold-degenerate bands are broken into two twofold-degenerate bands [see Fig. 7(b)], except for the fourfold-degenerate nodal lines along the *R*-*T*-*Z* direction, which are protected by a combination of glide-mirror and *PT* symmetries. Therefore, similar to other phases of carbides [19,25], β-Mo_2C with nodal lines crossing the Fermi level could also be material candidates for future studies of topological SC.

Among the 8 bands crossing the Fermi level, only two of them contribute significantly to the DOS and have the largest Fermi surfaces (FSs). These two bands are highlighted in purple and cyan in Fig. 8(a), and their corresponding FSs are depicted in Figs. 8(b) and 8(c), respectively. Clearly, these two bands form distinct FSs, even though both are due to Mo-4*d* orbitals. The purple band exhibits two small hole pockets near the Brillouin center, which are much smaller than the analogous electron pocket of the cyan band. Near the Brillouin boundary of the purple band two cylinder-like FSs extend along the Γ-*Z* direction. By contrast, in the cyan band, such FSs extend along the Γ-*Y* direction. Clearly, the FSs of the orthorhombic Mo_2C are more three-dimensional and more complex than those of the α-phase TMCs. In the

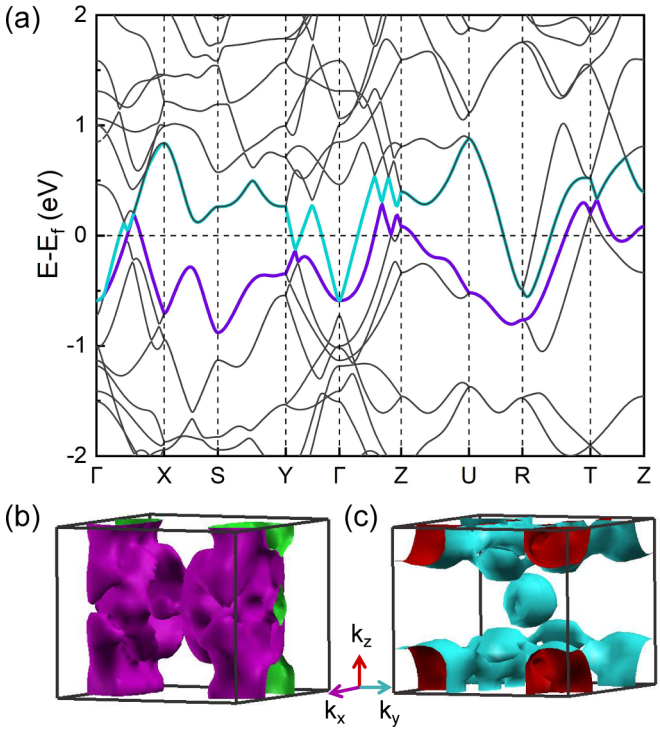

FIG. 8. (a) Close-up view of the electronic band structure without SOC for Mo_2C. The bands that cross the Fermi level are highlighted in purple and cyan. (b), (c) Representative Fermi surfaces of Mo_2C using the same color code for the bands as shown in panel (a).

latter case, the largest FSs consist of three cylinders along the k_i ($i = x, y, z$) directions. Such cylinder-like FSs originate from the strong hybridization between the transition-metal d orbitals and C-p orbitals. By contrast, the $p - d$ hybridization is rather weak in the orthorhombic Mo_2C. The cylinder-like FSs are known to play an important role in the SC of high-T_c iron-based materials [56–58]. This may also be the case for α-phase TMCs, which have relatively high T_c values in comparison to other carbide phases.

IV. DISCUSSION

Now, we briefly discuss the different phases of molybdenum carbides. To date, there are mainly two phases of molybdenum carbides that have been reported to become superconducting at low temperature, namely α-phase MoC_x and η-phase Mo_3C_2. The γ-phase MoC and ζ-phase Mo_2C adopt a noncentrosymmetric hexagonal and a centrosymmetric trigonal structure, respectively, but no SC has been reported in these phases yet. Recent theoretical work predicts that by introducing hole carriers, the γ-phase MoC could show SC with a T_c up to 9 K [19]. Here, by using the μSR technique, we reveal that it is the β-phase Mo_2C, instead, to represent the third member of molybdenum carbides to show bulk SC. Among the latter, the α and β phases show the highest and the lowest T_c, i.e., ∼15 K [29,30] and ∼3.2 K, respectively, while the η-phase Mo_3C_2 phase shows an intermediate T_c of 7.4 K [28]. The highest T_c in the α-phase TMCs is most likely due to their strong $p - d$ hybridization and, thus, to an enhanced electron-phonon coupling. We recall that the strong $p - d$ hybridization produces large cylinder-like FSs [19,25], which play an important role also in the SC of high-T_c iron-based materials [56–58]. As for the β-phase Mo_2C, band-structure calculations indicate a rather weak $p - d$ hybridization (see Fig. 7), which may justify their comparatively low T_c value.

The low-temperature superfluid density, determined by TF-μSR in our study, suggests a fully gapped superconducting state in the β-phase Mo_2C. A μSR study has not yet been performed in the α-phase MoC_x and η-phase Mo_3C_2. This is related to the difficulties in synthesizing sufficient amounts of material under the demanding conditions (1700 °C, 6–17 GPa) required in these cases [28–30]. According to our previous TF-μSR studies, the α-phase NbC and TaC also exhibit a fully gapped superconducting state [25]. We expect also the α-phase MoC_x to show similar SC properties to NbC and TaC. In fact, the electronic specific heat of α-phase MoC_x (and η-phase Mo_3C_2) shows an exponential temperature dependence in the superconducting state, consistent with a nodeless SC [28–30]. Further, the small zero-temperature energy gap ($\Delta_0 < 1.76\, k_B T_c$) and a reduced specific-heat jump at T_c ($\Delta C/\gamma T_c < 1.43$) suggest a weakly coupled SC in the various phases of superconducting molybdenum carbides. Taking into account the preserved TRS in the superconducting state, as well as an upper critical field H_{c2} well below the Pauli limit [25,28,29], we conclude that the molybdenum carbides exhibit a spin-singlet pairing, independent of their crystal structure (phase).

Finally, we discuss the topological aspects of molybdenum carbides. The α-phase MoC possesses a nonzero $\mathbb{Z}_2$ topological invariant and Dirac surface states [19]. The isostructural NbC contains three closed node lines in the bulk band structure (without considering SOC) of its first Brillouin zone. These are protected by time-reversal and space-inversion symmetries [25]. In case of a large SOC, such nodal loops become gapped. Since the 4d Nb and Mo atoms exhibit a weaker intrinsic SOC than the 5d Ta atoms, the SOC effects should be modest in both NbC and MoC. Consequently, the node lines—predicted by calculations neglecting SOC effects—are most likely preserved in both the above carbides. As such, the α-phase MoC and NbC might be good candidates for observing the exotic two-dimensional surface states. Further, although the γ-phase MoC is not superconducting in its pristine form, it is predicted to be a topological nodal-line material, exhibiting drumhead surface states. After introducing hole carriers, its SC can be tuned to reach a T_c of up to 9 K [19]. Since the γ-phase MoC adopts a noncentrosymmetric hexagonal structure, it can be classified as a topological Weyl semimetal. Indeed, three-component fermions were experimentally observed in the γ-phase MoP and WC [17,59]. By applying external pressure, the topological semimetal MoP becomes a superconductor, whose T_c reaches 4 K (above 90 GPa) [18], thus representing a possible candidate of topological superconductor. Here, we also find that the β-phase Mo_2C hosts twofold-degenerate nodal surfaces and fourfold-degenerate nodal lines near the Fermi level. In the case of SOC, the fourfold-degenerate nodal lines cross the Fermi level and, hence, could contribute to the superconducting pairing. In general, all the various phases of molybdenum carbides are promising for studying topological superconductivity.

V. CONCLUSION

To summarize, we studied the superconducting properties of Mo_2C mostly by means of the μSR technique, as well as via numerical band-structure calculations. The latter show that the phonon dispersion spectrum of Mo_2C provides the lowest total energy in the case of the orthorhombic β phase (with *Pbcn* space group), a result consistent with the experiment. Magnetization measurements confirm the bulk superconductivity of Mo_2C, with a T_c of 3.2 K. The temperature dependence of the superfluid density reveals a *nodeless* superconducting state, which is well described by an *isotropic s-wave* model. The lack of spontaneous magnetic fields below T_c indicates that time-reversal symmetry is *preserved* in the superconducting state of Mo_2C. Electronic band-structure calculations suggest that the density of states at the Fermi level is dominated by the Mo-4d electrons, while the contribution of the C-2p electrons is negligible over a broad energy range. As a consequence, the $p-d$ hybridization is rather weak in the β-phase Mo_2C, resulting in a relatively low T_c value. Topological nodal states including nodal surfaces and nodal lines could be identified in the Mo_2C electronic band structure near the Fermi level. This finding, together with the intrinsic superconductivity, suggests that the β-phase Mo_2C, too, is a potential candidate for studies of topological SC, similar to the other phases of molybdenum carbides.

ACKNOWLEDGMENTS

The authors thank Weikang Wu for fruitful discussions. This work was supported by the Natural Science Foundation of Shanghai (Grants No. 21ZR1420500 and No. 21JC1402300), the Natural Science Foundation of Chongqing (Grant No. CSTB-2022NSCQ-MSX1678), the National Natural Science Foundation of China (Grant No. 12374105), the Fundamental Research Funds for the Central Universities, and the Schweizerische Nationalfonds zur Förderung der Wissenschaftlichen Forschung (SNF) (Grants No. 200021_169455 and No. 200021_188706). We also acknowledge the allocation of beam time at the Swiss muon source (Dolly μSR spectrometer).

[1] X.-L. Qi and S.-C. Zhang, Topological insulators and superconductors, Rev. Mod. Phys. **83**, 1057 (2011).
[2] A. Y. Kitaev, Unpaired Majorana fermions in quantum wires, Phys. Usp. **44**, 131 (2001).
[3] C. Kallin and J. Berlinsky, Chiral superconductors, Rep. Prog. Phys. **79**, 054502 (2016).
[4] M. Sato and Y. Ando, Topological superconductors: A review, Rep. Prog. Phys. **80**, 076501 (2017).
[5] Y. S. Hor, A. J. Williams, J. G. Checkelsky, P. Roushan, J. Seo, Q. Xu, H. W. Zandbergen, A. Yazdani, N. P. Ong, and R. J. Cava, Superconductivity in $Cu_xBi_2Se_3$ and its implications for pairing in the undoped topological insulator, Phys. Rev. Lett. **104**, 057001 (2010).
[6] S. Sasaki, M. Kriener, K. Segawa, K. Yada, Y. Tanaka, M. Sato, and Y. Ando, Topological superconductivity in $Cu_xBi_2Se_3$, Phys. Rev. Lett. **107**, 217001 (2011).
[7] Z. Liu, X. Yao, J. Shao, M. Zuo, L. Pi, S. Tan, C. Zhang, and Y. Zhang, Superconductivity with topological surface state in $Sr_xBi_2Se_3$, J. Am. Chem. Soc. **137**, 10512 (2015).
[8] Y. Li and Z. Xu, Exploring topological superconductivity in topological materials, Adv. Quantum Technol. **2**, 1800112 (2019).
[9] R. M. Lutchyn, E. P. A. M. Bakkers, L. P. Kouwenhoven, P. Krogstrup, C. M. Marcus, and Y. Oreg, Majorana zero modes in superconductor-semiconductor heterostructures, Nat. Rev. Mater. **3**, 52 (2018).
[10] L. Fu and C. L. Kane, Superconducting proximity effect and Majorana fermions at the surface of a topological insulator, Phys. Rev. Lett. **100**, 096407 (2008).
[11] S.-Y. Xu, N. Alidoust, I. Belopolski, A. Richardella, C. Liu, M. Neupane, G. Bian, S.-H. Huang, R. Sankar, C. Fang, B. Dellabetta, W. Dai, Q. Li, M. J. Gilbert, F. Chou, N. Samarth, and M. Z. Hasan, Momentum-space imaging of Cooper pairing in a half-Dirac-gas topological superconductor, Nat. Phys. **10**, 943 (2014).
[12] J.-P. Xu, C. Liu, M.-X. Wang, J. Ge, Z.-L. Liu, X. Yang, Y. Chen, Y. Liu, Z.-A. Xu, C.-L. Gao, D. Qian, F.-C. Zhang, and J.-F. Jia, Artificial topological superconductor by the proximity effect, Phys. Rev. Lett. **112**, 217001 (2014).
[13] Y. Hu, S. M. Teicher, B. R. Ortiz, Y. Luo, S. Peng, L. Huai, J. Ma, N. C. Plumb, S. D. Wilson, J. He, and M. Shi, Topological surface states and flat bands in the kagome superconductor CsV_3Sb_5, Sci. Bull. **67**, 495 (2022).
[14] M. Sakano, K. Okawa, M. Kanou, H. Sanjo, T. Okuda, T. Sasagawa, and K. Ishizaka, Topologically protected surface states in a centrosymmetric superconductor $\beta-PdBi_2$, Nat. Commun. **6**, 8595 (2015).
[15] S.-Y. Guan, P.-J. Chen, M.-W. Chu, R. Sankar, F. Chou, H.-T. Jeng, C.-S. Chang, and T.-M. Chuang, Superconducting topological surface states in the noncentrosymmetric bulk superconductor $PbTaSe_2$, Sci. Adv. **2**, e1600894 (2016).
[16] L. E. Toth, *Transition Metal Carbides and Nitrides* (Academic Press, New York, 1971).
[17] J.-Z. Ma, J.-B. He, Y.-F. Xu, B. Q. Lv, D. Chen, W.-L. Zhu, S. Zhang, L.-Y. Kong, X. Gao, L.-Y. Rong, Y.-B. Huang, P. Richard, C.-Y. Xi, E. S. Choi, Y. Shao, Y.-L. Wang, H.-J. Gao, X. Dai, C. Fang, H.-M. Weng *et al.*, Three-component fermions with surface Fermi arcs in tungsten carbide, Nat. Phys. **14**, 349 (2018).
[18] Z. Chi, X. Chen, C. An, L. Yang, J. Zhao, Z. Feng, Y. Zhou, Y. Zhou, C. Gu, B. Zhang, Y. Yuan, C. Kenney-Benson, W. Yang, G. Wu, X. Wan, Y. Shi, X. Yang, and Z. Yang, Pressure-induced superconductivity in MoP, npj Quantum Mater. **3**, 28 (2018).
[19] A. Huang, A. D. Smith, M. Schwinn, Q. Lu, T.-R. Chang, W. Xie, H.-T. Jeng, and G. Bian, Multiple topological electronic phases in superconductor MoC, Phys. Rev. Mater. **2**, 054205 (2018).
[20] R. Zhan and X. Luo, Topologically nontrivial phases in superconducting transition metal carbides, J. Appl. Phys. **125**, 053903 (2019).

[21] E. I. Isaev, S. I. Simak, I. A. Abrikosov, R. Ahuja, Y. K. Vekilov, M. I. Katsnelson, A. I. Lichtenstein, and B. Johansson, Phonon related properties of transition metals, their carbides, and nitrides: A first-principles study, J. Appl. Phys. **101**, 123519 (2007).

[22] H. M. Tütüncü, S. Bağcı, G. P. Srivastava, and A. Akbulut, Electrons, phonons and superconductivity in rocksalt and tungsten-carbide phases of CrC, J. Phys.: Condens. Matter **24**, 455704 (2012).

[23] K. Kavitha, G. Sudha Priyanga, R. Rajeswarapalanichamy, and K. Iyakutti, Structural stability, electronic, mechanical and superconducting properties of CrC and MoC, Mater. Chem. Phys. **169**, 71 (2016).

[24] N. J. Szymanski, I. Khatri, J. G. Amar, D. Gall, and S. V. Khare, Unconventional superconductivity in 3*d* rocksalt transition metal carbides, J. Mater. Chem. C **7**, 12619 (2019).

[25] T. Shang, J. Z. Zhao, D. J. Gawryluk, M. Shi, M. Medarde, E. Pomjakushina, and T. Shiroka, Superconductivity and topological aspects of the rocksalt carbides NbC and TaC, Phys. Rev. B **101**, 214518 (2020).

[26] R. H. Willens, E. Buehler, and B. T. Matthias, Superconductivity of the transition-metal carbides, Phys. Rev. **159**, 327 (1967).

[27] W. S. Williams, Transition-metal carbides, Prog. Solid State Chem. **6**, 57 (1971), and references therein.

[28] K. Yamaura, Q. Huang, M. Akaishi, and E. Takayama-Muromachi, Superconductivity in the hexagonal-layered molybdenum carbide β-Mo_3C_2, Phys. Rev. B **74**, 184510 (2006).

[29] C. I. Sathish, Y. Guo, X. Wang, Y. Tsujimoto, J. Li, S. Zhang, Y. Matsushita, Y. Shi, H. Tian, H. Yang, J. Li, and K. Yamaura, Superconducting and structural properties of δ-$MoC_{0.681}$ cubic molybdenum carbide phase, J. Solid State Chem. **196**, 579 (2012).

[30] C. I. Sathish, Y. Shirako, Y. Tsujimoto, H. L. Feng, Y. Sun, M. Akaogi, and K. Yamaura, Superconductivity of δ-$MoC_{0.75}$ synthesized at 17 GPa, Solid State Commun. **177**, 33 (2014).

[31] Q. Mao, J. Yang, R. Li, H. Hao, Z. Lou, Y. Zhou, and M. Fang, Superconductivity in an arc melted MoC, Physica C **563**, 7 (2019).

[32] Y. Ge, H. Song, K. Bao, S. Ma, L. Li, Q. Tao, P. Zhu, B. Liu, D. Duan, and T. Cui, A novel hard superconductor obtained in dimolybdenum carbide (Mo_2C) with Mo-C octahedral structure, J. Alloys Compd. **881**, 160631 (2021).

[33] A. A. Suter and B. M. Wojek, Musrfit: A free platform-independent framework for μSR data analysis, Phys. Procedia **30**, 69 (2012).

[34] J. P. Perdew, K. Burke, and M. Ernzerhof, Generalized gradient approximation made simple, Phys. Rev. Lett. **77**, 3865 (1996).

[35] G. Kresse and J. Furthmüller, Efficient iterative schemes for *ab initio* total-energy calculations using a plane-wave basis set, Phys. Rev. B **54**, 11169 (1996).

[36] G. Kresse and J. Furthmüller, Efficiency of ab-initio total energy calculations for metals and semiconductors using a plane-wave basis set, Comput. Mater. Sci. **6**, 15 (1996).

[37] G. Kresse and D. Joubert, From ultrasoft pseudopotentials to the projector augmented-wave method, Phys. Rev. B **59**, 1758 (1999).

[38] P. E. Blöchl, Projector augmented-wave method, Phys. Rev. B **50**, 17953 (1994).

[39] X. Gonze and C. Lee, Dynamical matrices, Born effective charges, dielectric permittivity tensors, and interatomic force constants from density-functional perturbation theory, Phys. Rev. B **55**, 10355 (1997).

[40] A. Togo, L. Chaput, T. Tadano, and I. Tanaka, Implementation strategies in phonopy and phono3py, J. Phys.: Condens. Matter **35**, 353001 (2023).

[41] A. Togo, First-principles phonon calculations with phonopy and phono3py, J. Phys. Soc. Jpn. **92**, 012001 (2023).

[42] E. Rudy, C. E. Brukl, and S. Windisch, Constitution of ternary Ta-Mo-C alloys, J. Am. Ceram. Soc. **51**, 239 (1968).

[43] T. Epicier, J. Dubois, C. Esnouf, G. Fantozzi, and P. Convert, Neutron powder diffraction studies of transition metal hemicarbides M_2C_{1-x}—II. *In situ* high temperature study on W_2C_{1-x} and Mo_2C_{1-x}, Acta Metall. **36**, 1903 (1988).

[44] J. Rodríguez-Carvajal, Recent advances in magnetic structure determination by neutron powder diffraction, Phys. B: Condens. Matter **192**, 55 (1993).

[45] A. Yaouanc and P. D. de Réotier, *Muon Spin Rotation, Relaxation, and Resonance: Applications to Condensed Matter* (Oxford University Press, Oxford, 2011).

[46] A. Amato and E. Morenzoni, *Introduction to Muon Spin Spectroscopy: Applications to Solid State and Material Sciences* (Springer, Cham, 2024).

[47] S. J. Blundell, R. De Renzi, T. Lancaster, and F. L. Pratt (eds.), *Muon Spectroscopy: An Introduction* (Oxford University Press, Oxford, 2021).

[48] A. Maisuradze, R. Khasanov, A. Shengelaya, and H. Keller, Comparison of different methods for analyzing μSR line shapes in the vortex state of type-II superconductors, J. Phys.: Condens. Matter **21**, 075701 (2009), and references therein.

[49] W. Barford and J. M. F. Gunn, The theory of the measurement of the London penetration depth in uniaxial type II superconductors by muon spin rotation, Physica C **156**, 515 (1988).

[50] E. H. Brandt, Properties of the ideal Ginzburg-Landau vortex lattice, Phys. Rev. B **68**, 054506 (2003).

[51] M. Tinkham, *Introduction to Superconductivity*, 2nd ed. (Dover Publications, Mineola, NY, 1996).

[52] A. Carrington and F. Manzano, Magnetic penetration depth of MgB_2, Physica C **385**, 205 (2003).

[53] R. Kubo and T. Toyabe, A stochastic model for low field resonance and relaxation, in *Magnetic Resonance and Relaxation*, edited by R. Blinc (North-Holland, Amsterdam, 1967), pp. 810–823.

[54] Y. Liu, Y. Jiang, J. Feng, and R. Zhou, Elasticity, electronic properties and hardness of MoC investigated by first principles calculations, Phys. B: Condens. Matter **419**, 45 (2013).

[55] Z.-M. Yu, Z. Zhang, G.-B. Liu, W. Wu, X.-P. Li, R.-W. Zhang, S. A. Yang, and Y. Yao, Encyclopedia of emergent particles in three-dimensional crystals, Sci. Bull. **67**, 375 (2022).

[56] I. I. Mazin, D. J. Singh, M. D. Johannes, and M. H. Du, Unconventional superconductivity with a sign reversal in the order parameter of $LaFeAsO_{1-x}F_x$, Phys. Rev. Lett. **101**, 057003 (2008).

[57] K. Kuroki, H. Usui, S. Onari, R. Arita, and H. Aoki, Pnictogen height as a possible switch between high-T_c nodeless and low-T_c nodal pairings in the iron-based superconductors, Phys. Rev. B **79**, 224511 (2009).

[58] I. I. Mazin, M. Shimizu, N. Takemori, and H. O. Jeschke, Novel Fe-based superconductor $LaFe_2As_2$ in comparison

with traditional pnictides, Phys. Rev. Lett. **123**, 267001 (2019).

[59] B. Q. Lv, Z.-L. Feng, Q.-N. Xu, X. Gao, J.-Z. Ma, L.-Y. Kong, P. Richard, Y.-B. Huang, V. N. Strocov, C. Fang, H.-M. Weng, Y.-G. Shi, T. Qian, and H. Ding, Observation of three-component fermions in the topological semimetal molybdenum phosphide, Nature (London) **546**, 627 (2017).